Effects of wind veer on a yawed wind turbine wake in atmospheric boundary layer flow

Ghanesh Narasimhan, Dennice F. Gayme, and Charles Meneveau
Department of Mechanical Engineering, Johns Hopkins University, Baltimore, Maryland 21218, USA

(Received 9 June 2022; accepted 25 October 2022; published 28 November 2022)

Large eddy simulations (LESs) are used to study the effects of veer (the height-dependent lateral deflection of wind velocity due to Coriolis acceleration) on the evolution of wind turbine wakes in the atmospheric boundary layer. Specifically, this work focuses on turbines that are yawed with respect to the mean incoming wind velocity, which produces laterally deflected wakes that have a curled (crescent-shaped) structure. These effects can be attributed to the introduction of streamwise mean vorticity and the formation of a counter-rotating vortex pair (CVP) on the top and bottom of the wake. In a truly neutral boundary layer (TNBL) in which wind veer effects are absent, these effects can be captured well with existing analytical wake models [Bastankhah *et al.*, J. Fluid Mech. **933**, A2 (2022)]. However, in the more realistic case of atmospheric boundary layers subjected to Coriolis acceleration, existing models need to be reexamined and generalized to include the effects of wind veer. To this end, the flow in a conventionally neutral atmospheric boundary layer (CNBL) interacting with a yawed wind turbine is investigated in this paper. Results indicate that in the presence of veer the CVP's top and bottom vortices exhibit considerable asymmetry. However, upon removing the veer component of vorticity, the resulting distribution is much more symmetric and agrees well with that observed in a TNBL. These results are used to develop a simple correction to predict the mean velocity distribution in the wake of a yawing turbine in a CNBL using analytical models. The correction includes the veer-induced sideways wake deformation, as proposed by Abkar *et al.* [Energies **11**, 1838 (2018)]. The resulting model predictions are compared with mean velocity distributions from the LESs, and good agreement is obtained.

DOI: 10.1103/PhysRevFluids.7.114609

I. INTRODUCTION

Yawing a turbine deflects its wake, decreasing wake interactions and potentially increasing the power output of downstream turbines [1]. Coordinating such actions over a wind farm could improve its overall efficiency [2]. Wake deflection due to yaw was studied experimentally in [3–7], while Ref. [8] performed an early large eddy simulation (LES) study and proposed a simple analytical model for predicting the initial wake skewing angle just behind the turbine. In a subsequent wind tunnel study [9], the formation of an axial counter-rotating vortex pair (CVP) was observed behind a yawed actuator disk, in the presence of a uniform inflow. The deflection of the wake was attributed to the CVP because the vortices (one above and the other below the actuator disk) induce a side wash velocity that deflects the wake from the center of the turbine. The vortices also deform the wake shape into a curled (crescent-shaped) structure. Reference [10] performed further wind tunnel studies of a model wind turbine in a turbulent boundary layer and also observed CVP formation.

Reference [11] proposed considering the turbine as a lifting surface (applying a height-dependent sideways force onto the fluid), analogous to a vertically placed airfoil that sheds streamwise (tip) vortices in the presence of an incoming mean flow. Evaluation of the induced strength of the CVP

near the turbine enabled predicting the yaw-induced wake deflection quite accurately [11]. Other vortex-based models describe the vorticity at the turbine as a distribution of multiple, discrete point vortices [12–14] whose downstream transport and diffusion are modeled numerically. Following these studies, Ref. [15] proposed a theory for the generation and downstream evolution of the CVP. Their analytical predictions for the decay of the maximum vorticity and circulation strength of the vortices showed very good agreement with the LES data, while still assuming a circular shape of the wake. In a more detailed recent study [16], it was shown that an analytical vortex-sheet-based model can successfully predict the curled wake shape behind yawed turbines. In this model, the wake edge was treated as a vortex sheet, and analytical solutions for the wake shape were obtained using truncated power series expansions and the decaying circulation strength estimate of the CVP from Ref. [15]. In addition, the lateral deflection of the wake induced by the trailing vortices was also modeled. The Gaussian wake model for the axial velocity deficit in Ref. [16] was then modified to include the deformation caused by the vortex sheet and this combined model predicted the curled shape and the deflection of the wake quite accurately.

Wind turbine wake properties and the performance of wind farms depend on the prevailing properties of the atmospheric boundary layer (ABL). For instance, it is well known that the wake recovery rate (i.e., the wake expansion coefficient) is affected by the ABL's thermal stratification conditions [17]. At the same time, the Coriolis acceleration due to Earth's rotation causes an Ekman spiral flow in the surface layer of the ABL [18]. This leads to a height-dependent lateral realignment of the incoming wind direction called wind veer, which can significantly affect the wind farm power output [19]. Veer effects have been previously considered for an unyawed turbine in a stably stratified ABL [20]. That work modified the Gaussian wake model with a veer correction term which successfully predicted the skewed or sheared wake structure arising from the spanwise shear due to the wind veer. Reference [21] considered the effects of both yaw and veer on individual turbine blade aerodynamics. However, the combined effects of veer and yawing on wind turbine wakes and their modeling via analytical approaches have not yet received significant attention so far. The objective of the present study is to examine the evolution of turbine wakes in the presence of both turbine yawing and veer, as well as to include both of these effects in analytical models of the turbine wake.

In order to generate the relevant data, an LES of a yawed wind turbine in the presence of an incoming mean flow typical of a conventionally neutral ABL (CNBL) that includes veer is performed. The CNBL is a type of ABL characterized by a neutrally stratified turbulent boundary layer region separated from the geostrophic and stably stratified free atmosphere by a capping inversion layer at the boundary layer height [22]. As a reference, we also perform an LES of a yawed wind turbine in a truly neutral boundary layer (TNBL) in which veer effects are absent. The details of the LESs are described in Sec. II. The results are analyzed in Sec. III, which focuses on the effect of wind veer on the downstream evolution of mean vorticity. The results are used to introduce modifications to existing analytical models so that both ABL veer and turbine yaw can be represented efficiently and accurately as described in Sec. IV. The main conclusions are summarized in Sec. V.

II. LARGE EDDY SIMULATION OF A YAWED WIND TURBINE IN A CNBL

This section details the LES setup of CNBL and TNBL simulations used to generate data to study the effect of wind veer on a yawed turbine wake. We use the open-source code LESGO [23], an LES solver primarily developed to simulate ABL flows [24,25]. The code includes various dynamic subgrid stress parametrizations, wall models, wind turbine representations using actuator disk or line models, and inflow generation using the concurrent-precursor approach [26]. The code has been validated by several previous studies [11,15,25–31]. The governing equations and numerical method, initial conditions for the velocity, and potential temperature are discussed in Sec. II A. The simulation setup is described in Sec. II B. The characteristics of the CNBL and TNBL to be

simulated are described in Sec. II C, which documents the main differences in the mean flow velocity profiles between the two cases.

A. Governing equations and numerical method

The code LESGO solves the filtered Navier-Stokes equations (with the Boussinesq approximation for buoyancy effects) and the scalar potential temperature transport equation:

$$\frac{\partial \tilde{u}_i}{\partial x_i} = 0, \tag{1}$$

$$\frac{\partial \tilde{u}_i}{\partial t} + \tilde{u}_j\left(\frac{\partial \tilde{u}_i}{\partial x_j} - \frac{\partial \tilde{u}_j}{\partial x_i}\right) = -\frac{1}{\rho_0}\frac{\partial p_\infty}{\partial x_i} - \frac{\partial \tilde{p}}{\partial x_i} + \frac{g}{\tilde{\theta}_0}(\tilde{\theta} - \tilde{\theta}_0)\delta_{i3} - \frac{\partial \tau_{ij}}{\partial x_j} + \frac{1}{\rho_0}\tilde{f}_x\delta_{i1} + \frac{1}{\rho_0}\tilde{f}_y\delta_{i2} - f_c\tilde{u}\delta_{i2} + f_c\tilde{v}\delta_{i1} \tag{2}$$

$$\frac{\partial \tilde{\theta}}{\partial t} + \tilde{u}_j\frac{\partial \tilde{\theta}}{\partial x_j} = -\frac{\partial \Pi_j}{\partial x_j} \tag{3}$$

where the tilde $(\tilde{\cdot})$ represents spatial filtering operation such that $\tilde{u}_i = (\tilde{u}, \tilde{v}, \tilde{w})$ are the filtered velocity components in the streamwise (x), lateral (y), and vertical (z) directions, respectively, and $\tilde{\theta}$ is the filtered potential temperature. The term $\tau_{ij} = \sigma_{ij} - (1/3)\sigma_{kk}\delta_{ij}$ is the deviatoric part of the subgrid scale (SGS) stress tensor $\sigma_{ij} = \widehat{u_i u_j} - \tilde{u}_i\tilde{u}_j$. The quantity $\tilde{p} = \tilde{p}_*/\rho_0 + (1/3)\sigma_{kk} + (1/2)\tilde{u}_j\tilde{u}_j$ is the modified pressure, where the actual pressure $\tilde{p}_*$ divided by the ambient density ρ_0 is augmented with the trace of the SGS stress tensor and the kinematic pressure arising from writing the nonlinear terms in rotational form. The quantities $\tilde{f}_i = (\tilde{f}_x, \tilde{f}_y, 0)$ are the streamwise and spanwise components of the turbine's force imparted on the fluid. The term $-(1/\rho_0)\partial p_\infty/\partial x_i$ is the mean external pressure gradient applied to drive the flow. The δ_{ij} in Eq. (2) is the Kronecker delta function determining the direction of buoyancy, turbine thrust, and Coriolis forces. In the buoyancy term, $g = 9.8$ m/s^2 is the gravitational acceleration, and $\tilde{\theta}_0$ is the reference potential temperature scale taken to be 288 K for the CNBL case. In the Coriolis force terms, $f_c = 2\Omega\sin\phi = 10^{-4}$ s^{-1} is the Coriolis parameter at latitude $\phi = 45^\circ$. In Eq. (3), the term $\Pi_j = u_j\theta - \tilde{u}_j\tilde{\theta}$ is the SGS heat flux.

In the momentum equation (2) a constant mean pressure gradient $\nabla p_\infty = (\partial p_\infty/\partial x, \partial p_\infty/\partial y, 0)$ is applied to drive the flow. For the CNBL case, it is written in terms of the geostrophic velocity components U_g, V_g using the geostrophic balance equation

$$\frac{1}{\rho_0}\frac{\partial p_\infty}{\partial x} = f_c V_g, \quad \frac{1}{\rho_0}\frac{\partial p_\infty}{\partial y} = -f_c U_g. \tag{4}$$

The geostrophic velocity components are specified as $U_g = G\cos\alpha$, $V_g = G\sin\alpha$, where $G = (U_g^2 + V_g^2)^{1/2}$ is the magnitude of the geostrophic wind, which is set to 8 m/s, and α is the angle made by the resultant wind velocity vector with respect to the streamwise x direction. For the TNBL case, the dimensionless streamwise mean pressure gradient is set to a constant value. This constant streamwise pressure gradient ensures that the mean flow is streamwise aligned throughout the domain without any wind veer [$V(z) \equiv 0$]. In addition, since the TNBL flow is isothermal and neutrally buoyant throughout the domain, Eq. (3) is not solved for this case, and the buoyancy term in the momentum equation (2) vanishes.

In the CNBL simulation, we maintain a mean flow direction such that it is streamwise aligned at the hub height. This is achieved by choosing a value of α for the geostrophic wind such that the wind veer at hub height is zero [$V(z = 0) = 0$]. To compute the appropriate value of α, we use the proportional-integral (PI) control approach introduced in Ref. [32] with a proportional gain $K_P = 10$ and an integral gain $K_I = 0.5$. We also impose the constraint $V(z = 0) = 0$.

We solve the equations for the high Reynolds number limit such that the molecular viscous and heat diffusion terms are neglected in Eqs. (2) and (3). The necessary diffusion for the problem is provided by modeling the deviatoric part of the SGS stress tensor (τ_{ij}) and the SGS heat flux (Π_j)

as

$$\tau_{ij} = -2\nu_T^{\mathrm{SGS}}\tilde{S}_{ij}, \quad \Pi_j = -\kappa_T^{\mathrm{SGS}}\frac{\partial\tilde{\theta}}{\partial x_j}, \tag{5}$$

where ν_T^{SGS} is the SGS momentum diffusivity, κ_T^{SGS} is the SGS heat diffusivity, and $\tilde{S}_{ij} = (1/2)(\partial\tilde{u}_i/\partial x_j + \partial\tilde{u}_j/\partial x_i)$ is the symmetric part of the velocity gradient tensor. The diffusivities are related by the SGS Prandtl number $\mathrm{Pr}_{\mathrm{SGS}} = \nu_T^{\mathrm{SGS}}/\kappa_T^{\mathrm{SGS}}$, which is taken to be 0.4 in this paper [33]. The diffusivities ν_T^{SGS} and κ_T^{SGS} are modeled as

$$\nu_T^{\mathrm{SGS}} = (C_S\tilde{\Delta})^2\sqrt{\tilde{S}_{ij}\tilde{S}_{ij}}, \quad \kappa_T^{\mathrm{SGS}} = \mathrm{Pr}_{\mathrm{SGS}}^{-1}\nu_T^{\mathrm{SGS}} = \mathrm{Pr}_{\mathrm{SGS}}^{-1}(C_S\tilde{\Delta})^2\sqrt{\tilde{S}_{ij}\tilde{S}_{ij}}, \tag{6}$$

where C_S is the Smagorinsky model coefficient and $\tilde{\Delta} = (\Delta x\Delta y\Delta z)^{1/3}$ is the filter width and Δx, Δy, Δz are the respective x, y, z grid spacings. The model coefficient C_S is evaluated using the Lagrangian dynamic scale-dependent model [25].

The code uses the pseudospectral method along the streamwise and spanwise directions. The wall-normal direction is discretized using a second-order central finite difference method. The second-order accurate Adams-Bashforth scheme is used for time advancement. A shifted periodic boundary condition is used in the streamwise direction of the precursor domain to prevent artificially long flow structures from developing. This approach also enables the development of statistical homogeneity with a shorter precursor domain size and less computational cost [34]. A stress-free boundary condition is imposed on the top boundaries of the domains. The wall stress boundary condition from the equilibrium wall model is applied at the bottom wall of both the precursor and wind turbine domains. Assuming that the grid points near the surface are within the logarithmic layer (Monin-Obukhov similarity in the absence of stratification), the wall stress τ_w magnitude is evaluated as

$$\tau_w = -\left(\frac{\tilde{u}_r\kappa}{\ln(z_1/z_0)}\right)^2, \tag{7}$$

where $\tilde{u}_r = \sqrt{\tilde{u}^2 + \tilde{v}^2}$ is the resultant horizontal velocity at the first grid point $z = z_1 = \Delta z/2$, $\kappa = 0.41$ is the von Kármán constant, and $z_0 = 0.1$ m is the assumed surface roughness height. Using Eq. (7), the wall stress components are evaluated as

$$\tau_{i,3|w} = \tau_w\frac{\tilde{u}_i}{\tilde{u}_r}, \quad i = 1, 2, \tag{8}$$

which are applied as the stress boundary conditions at the bottom boundary. For the CNBL simulation, we apply a zero-buoyancy-flux boundary condition $q_* = 0$ to maintain neutral stratification within the ABL.

The velocity fields of both the CNBL and TNBL LES are initialized with a log-law velocity profile with zero-mean white noise superimposed. The noise is initialized for the entire domain in the TNBL while only for the first 900 m from the bottom surface for the CNBL. To simulate the CNBL conditions in the LES, an initial potential temperature profile with a capping inversion layer is set up such that the boundary layer is neutral below the layer and is stably stratified above it (see Fig. 1). The capping inversion height is set to 1 km from the ground. The initial potential temperature $\tilde{\theta}$ magnitude below the capping inversion region is 288 K (the same as the reference temperature scale $\tilde{\theta}_0$). The thickness of the capping inversion layer, where the potential temperature increases linearly from 288 to 290.5 K, is 100 m. Above this capping inversion layer, the potential temperature increases with a lapse rate of 0.001 K/m.

To represent the wind turbine, we use the local-thrust-coefficient-based actuator disk model (ADM) [15,27,31,35]. The ADM treats the turbine as a drag disk of diameter D and radius $R = D/2$ imparting a total force T on the fluid directed along the unit-normal direction $\boldsymbol{n} = \cos\beta\boldsymbol{i} + \sin\beta\boldsymbol{j}$

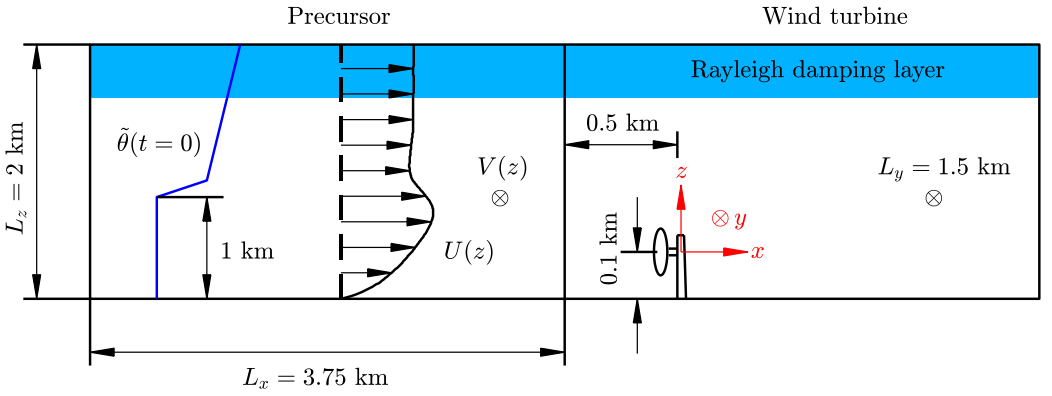

FIG. 1. Schematic of the CNBL simulation setup with the turbine in the concurrent wind turbine domain, inflow mean velocity profile with streamwise $U(z)$ and wind veer $V(z)$ components, and initial potential temperature profile $\tilde{\theta}(t=0)$ in the precursor domain.

perpendicular to the disk, where β is the yaw angle (see Fig. 2), and

$$T = -\frac{1}{2}\rho_0 \pi R^2 C_T' u_d^2. \tag{9}$$

Here, C_T' is the local thrust coefficient and u_d is the disk-averaged velocity defined as

$$u_d = \int \tilde{\boldsymbol{u}} \cdot \boldsymbol{n}\, \mathcal{R}(\boldsymbol{x}) d^3\boldsymbol{x} \; = \int (\tilde{u}\cos\beta + \tilde{v}\sin\beta)\mathcal{R}(\boldsymbol{x}) d^3\boldsymbol{x}. \tag{10}$$

The u_d is an average of the velocity in the direction normal to the disk, $\tilde{\boldsymbol{u}} \cdot \boldsymbol{n} = \tilde{u}\cos\beta + \tilde{v}\sin\beta$ with the integration performed over the actuator disk using the indicator function $\mathcal{R}(\mathbf{x})$ (defined below). The local thrust coefficient is set to $C_T' = 1.33$, the same value as used in previous studies [15,27,31,35] to represent standard wind turbine operating conditions. The force is spatially distributed using the smoothed indicator function $\mathcal{R}(\boldsymbol{x})$ such that the filtered force vector is

$$\tilde{\boldsymbol{f}} = T\,\mathcal{R}(\boldsymbol{x})\,\boldsymbol{n} = T\,\mathcal{R}(\boldsymbol{x})\cos\beta\,\boldsymbol{i} + T\,R(\boldsymbol{x})\sin\beta\,\boldsymbol{j}. \tag{11}$$

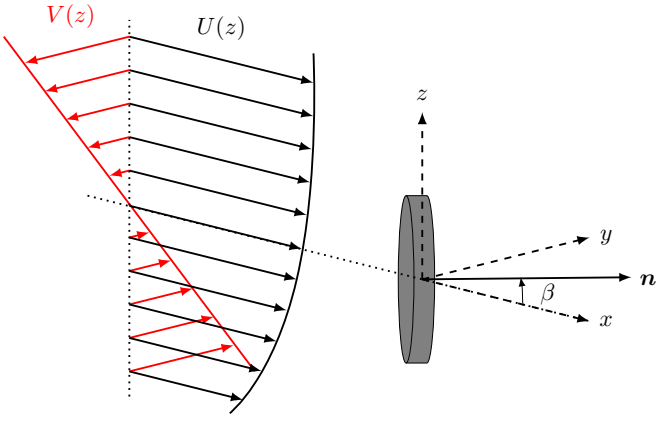

FIG. 2. Schematic sketch of an isometric view of a yawed wind turbine at angle β in the presence of ABL flow with mean velocity $\boldsymbol{U} = U(z)\boldsymbol{i} + V(z)\boldsymbol{j}$.

TABLE I. Computational domain size and grid points for LES of yawed wind turbine in the CNBL and TNBL cases. Note that the grid resolution is the same for both LES domains.

Case	Precursor and wind turbine domain size $[L_x$ (km)$\times L_y$ (km)$\times L_z$ (km)$]$	Number of grid points $(N_x \times N_y \times N_z)$	Grid resolution $[\Delta x$ (m)$\times \Delta y$ (m)$\times \Delta z$ (m)$]$
CNBL	$3.75\times1.5\times2$	$360\times144\times432$	$10.4\times10.4\times4.6$
TNBL	$3.75\times1.5\times1$	$360\times144\times216$	$10.4\times10.4\times4.6$

The smoothed indicator function is defined as [23,31]

$$\mathcal{R}(\boldsymbol{x}) = \int G(\boldsymbol{x}-\boldsymbol{x}')\mathcal{I}(\boldsymbol{x}')d^3\boldsymbol{x}', \tag{12}$$

where $\mathcal{I}(\boldsymbol{x})$ and $G(\boldsymbol{x})$ are the normalized indicator function and Gaussian filtering kernel, respectively, given by

$$\mathcal{I}(\boldsymbol{x}) = \frac{1}{s\pi R^2}[H(x+s/2) - H(x-s/2)]H(R-r), \tag{13}$$

$$G(\boldsymbol{x}) = \left(\frac{6}{\pi\Delta^2}\right)^{3/2} \exp\left(-6\frac{\|\boldsymbol{x}\|^2}{\Delta^2}\right). \tag{14}$$

In Eq. (13), s is the x-direction thickness of the forcing region, which is set to 10 m, and $H(x)$ is the Heaviside function, which is used to localize the disk within the region $-s/2 < x < s/2$ and $r < R$, where $r = \sqrt{y^2+z^2}$. In the filtering kernel (14), Δ is the filter width defined as $\Delta = 1.5h$, where $h = \sqrt{\Delta x^2 + \Delta y^2 + \Delta z^2}$ is the effective grid size.

We note that the actuator line model (ALM) is a high-fidelity representation of the turbine as it can capture the effects of root and tip vortices behind the turbine which are not resolved by the ADM. However, owing to the high computational costs of running LESs with ALM and because there are not many differences in the far-wake behavior between LES with the ADM and ALM [36], we choose the ADM over the ALM in this paper.

In the following sections, the simulation setup and results from the precursor simulation of the CNBL and TNBL LES cases are discussed.

B. Simulation setup

As shown in the schematic in Fig. 1, the simulation is performed using two computational domains, the precursor and wind turbine domains. The turbine is placed in the wind turbine domain while the turbulent inflow simulating the CNBL or TNBL conditions is generated in the precursor domain. The details of the domain size and number of grid points are summarized in Table I, and relevant dimensions are also shown in Fig. 1.

Figure 1 includes a sketch of the initial potential temperature ($\tilde{\theta}$) profile (blue line) used to simulate the CNBL atmospheric condition in the precursor domain. A sponge (or Rayleigh damping) layer at the top boundary is used to dampen gravity waves in the computational domain. This is a wave absorbing layer that is 500 m wide extending from the top boundary. A body force with a cosine profile for its damping coefficient is applied in this layer to prevent reflection of gravity waves [37,38]. The resultant mean flow is expected to take the form of a low-level jet with velocity $\boldsymbol{U} = U(z)\boldsymbol{i} + V(z)\boldsymbol{j}$. Together with the turbulence that develops in the precursor domain, the velocity is then used as an inflow for the wind turbine domain using the concurrent-precursor method [26]. In this method, at each time step, a part of flow from the precursor domain is copied to the outflow region of the wind turbine domain. A fringe region is then defined to smoothly transition between the wind turbine flow and the region of flow copied from the precursor domain. The direction of the incoming mean velocity changes as a function of height. In contrast, for the

TNBL simulation, the flow is isothermal in the entire computational domain, and there is no wind veer, i.e., $V(z) \equiv 0$.

The wind turbine domain (second downstream domain in Fig. 1) includes a single turbine yawed at an angle $\beta = 20^\circ$ placed at a distance of 500 m from the inlet. The diameter D and hub height z_h of the turbine are both 100 m. We use a Cartesian $(x\,y\,z)$ coordinate system centered at the hub of the turbine. Figure 2 provides a sketch of the turbine orientation indicating the yaw angle β, and the normal direction. Figure 2 also shows the two-component velocity profile that includes a veer velocity profile $V(z)$ in addition to the streamwise profile $U(z)$.

C. Characteristics of CNBL and TNBL

Upon reaching statistically stationary conditions, mean velocity profiles are obtained from the LES in the precursor domain by performing time t and horizontal spatial (x-y) averaging. Results are shown in Fig. 3 for both the CNBL (blue solid curves) and TNBL (open circles) cases. At the hub height, the magnitude of the mean velocity for the CNBL profile is $U_h = \sqrt{U^2(z=0) + V^2(z=0)} = 6.4$ m/s, and the pressure gradient forcing for the TNBL is set so that the same $U_h = 6.4$ m/s is implied for both simulations. The friction velocities obtained from averaging the wall stress in the precursor domain of both cases are $u_\tau = 0.35$ m/s. The resultant velocity profiles for the CNBL and TNBL are shown in Fig. 3(a) together with the log-law velocity profile. Both LES cases have a similar mean wind profile within the turbulent boundary layer. The streamwise $U(z)$ and spanwise wind veer component $V(z)$ of the CNBL flow are plotted in Figs. 3(b) and 3(c). The normalized streamwise velocities U/U_h from both the CNBL and TNBL cases agree quite well with each other. As expected, the TNBL case does not display any mean wind veer [open circles in Fig. 3(c)]. Conversely, wind veer exists in the CNBL. This veer is well represented as $V(z) = -Sz$ in the region near the turbine hub height, i.e., covering the rotor region between $z = 0.5D$ and $z = -0.5D$. We find from LES that the magnitude of the slope of the veer velocity is $S = 2.2\times10^{-3}$ s^{-1}. The Ekman spiral formed by $U(z)$ and $V(z)$ in the CNBL is shown in the inset of Fig. 3(b). These results confirm that a streamwise aligned mean flow is achieved at the hub height [$V(z=0) = 0$] for the CNBL (Fig. 2) using the proportional-integral (PI) controller approach [32]. This behavior is also evident in the plot of flow angle $\alpha(z) = \tan^{-1}[V(z)/U(z)]$ versus wall-normal height in Fig. 3(d), where $\alpha(z=0) = 0$. The corresponding plot (open circles) from the TNBL confirms that the flow is aligned in the streamwise direction throughout the domain height.

Figure 4 shows contour plots of time-averaged streamwise vorticity $\overline{\omega}_x$ for cross-stream planes at $x/D = [2, 6, 10, 14]$ from the TNBL and CNBL simulations. The vorticity and the streamlines overlaid on top of the TNBL contours at the cross planes indicate the presence of counter-rotating vortices in the wake region. There is a clearly visible clockwise rotating vortex below and counter-clockwise rotating vortex on top of the turbine as viewed along the positive x direction in Fig. 4(a). In contrast, for the CNBL case in Fig. 4(b), the contours show the presence of counter-rotating vortices affected significantly by the background veer vorticity where the top vortex is less visible than the bottom vortex.

The decay of the wake strength is displayed in Fig. 5, which shows the maximum velocity deficit $\Delta u_{\max}$ normalized by U_h in the wakes of the CNBL (blue curve) and TNBL cases (open circles) as a function of downstream distance from the turbine. Except for the near-rotor region ($x/D < 3$) they are very similar and also agree well with values obtained from a model (black curve) to be discussed later in Sec. IV.

In the next section, the time-averaged LES data are used to study the evolution and decay of the mean streamwise vorticity.

III. GENERATION AND DOWNSTREAM EVOLUTION OF MEAN VORTICITY

In this section, we discuss the implications of including the wind veer effects on the model developed in Ref. [15]. The model is based on the linearized mean streamwise vorticity equation and includes two mechanisms: (1) Streamwise vorticity is generated at the turbine due to curl of the

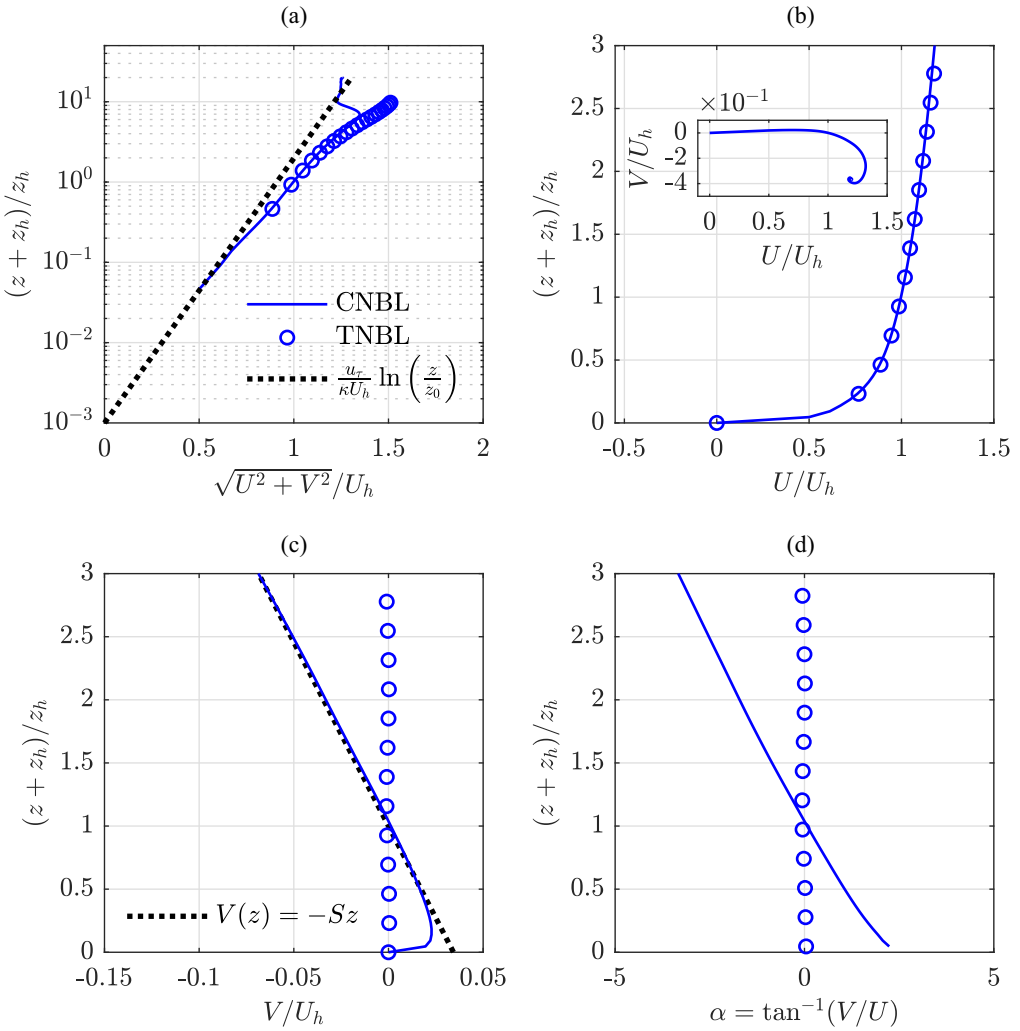

FIG. 3. Plots of (a) mean inflow velocity, (b) streamwise velocity, (c) spanwise or wind veer velocity, and (d) angle of the inflow near the hub height of the CNBL (blue solid curves) and TNBL (open circles) LES cases. The inset in (b) shows the Ekman spiral. The black dotted line in (a) corresponds to the log-law velocity profile with $u_\tau = 0.35$ m/s and $U_h = 6.4$ m/s. The black dotted line in (c) represents the linear approximation $V(z) = -Sz$ with $S = 2.2\times10^{-3}$ s^{-1}.

spanwise component of the thrust force, addressed in Sec. III A, and (2) the generated vorticity is advected downstream by the mean flow with simultaneous turbulent diffusion in the transverse y-z plane, discussed in Sec. III B.

A. Mean streamwise vorticity generation at the yawed rotor

At the turbine location, the spanwise component of the force due to the yawed turbine changes along the spanwise direction. As a result, streamwise mean vorticity is created at the actuator disk periphery which is then transported downstream eventually forming the CVP. At the rotor location, the linearized mean streamwise vorticity equation is dominated by advection and the creation of

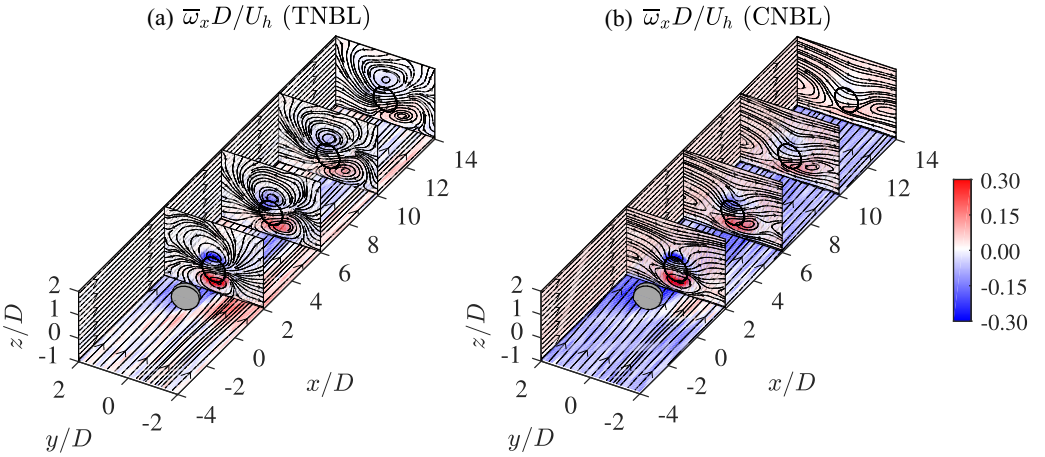

FIG. 4. Contours of time-averaged streamwise vorticity $\overline{\omega}_x$ behind a yawed wind turbine at angle $\beta = 20^\circ$ from the (a) TNBL and (b) CNBL simulations. Contours are shown on various downstream planes at locations $x/D = [2, 6, 10, 14]$ and on the bottom surface (first plane above the ground) and side plane at $y/D = 2$. The vorticity contours are normalized by the turbine diameter D and the hub height velocity U_h of the incoming mean flow. The streamlines of the flow on the planes shown are overlaid on top of the contours visibly showing the presence of the cross-stream flow.

vorticity due to the yawed actuator disk [15,39]:

$$U_h \frac{\partial \omega_x}{\partial x} = -\frac{1}{\rho_0}\frac{\partial f_y}{\partial z}, \tag{15}$$

where ω_x represents the time-averaged streamwise vorticity and f_y is the spanwise (y-direction) force per unit volume exerted by the turbine rotor on the passing air.

For a yawed actuator disk representation of the turbine, the spanwise component of the thrust force per unit (fluid) mass is given by [15]

$$f_y(x, y, z) = -\frac{1}{2}\rho_0 C_T U_h^2 \cos^2\beta\, H(R - r)\delta(x)\sin\beta, \tag{16}$$

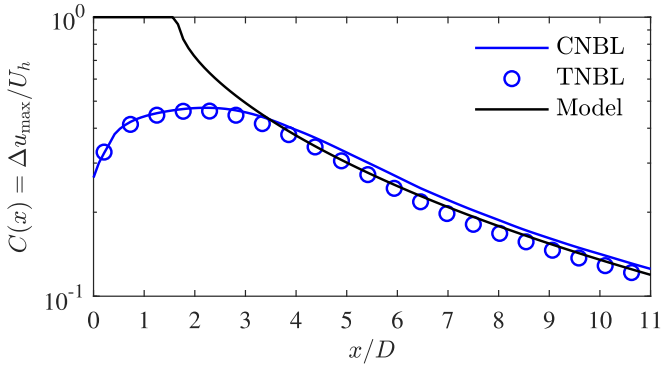

FIG. 5. Streamwise evolution of $C(x) = \Delta u_{\max}/U_h$, the maximum velocity deficit normalized by U_h in the wake of a yawed wind turbine for the CNBL case (blue solid curve) and TNBL case (open circles), compared with $C(x)$ from the model in Eq. (40) discussed in Sec. IV [black curve; the model is valid downstream of the near rotor region (i.e., for $x/D > 3$)].

where $r^2 = y^2 + z^2$. Equation (16) is obtained using the standard expression for total thrust force $T = -(1/2)\rho_0 \pi R^2 C_T U_h^2 \cos^2\beta$ distributed uniformly on the actuator disk. This distribution is represented using the indicator function $\mathcal{R}(\boldsymbol{x}) = H(R-r)\delta(x)/\pi R^2$ [11], where $H(R-r)$ is the Heaviside function with the radial coordinate r spanning the transverse y-z plane with its origin at the hub of the turbine. The force acts only at the turbine's streamwise position $x = 0$ as represented by the delta function $\delta(x)$. The thrust coefficient C_T in Eq. (16) is related to the local thrust coefficient C_T' in Eq. (9) by the relation $C_T = 16C_T'/(4 + C_T' \cos^2\beta)^2$ [11].

Using expression (16) in (15), the analytical form of the vorticity distribution generated at the turbine is obtained by integrating (15) in x, which gives

$$\omega_x(x=0, r, \theta) = -\frac{1}{\rho_0 U_h}\int_{-\infty}^{x} \frac{\partial f_y}{\partial z}\, dx = -\frac{1}{2} C_T U_h \cos^2\beta \sin\beta \sin\theta\, \delta(r-R) H(x). \tag{17}$$

Here, the r and θ directions are obtained through a cylindrical coordinate transformation of the y-z transverse plane defined by $y = r\cos\theta$ and $z = r\sin\theta$. The corresponding circulation strength of the top and bottom vortices can be obtained by integrating Eq. (17) for the top and bottom half planes, respectively, which gives

$$\Gamma_{\text{top}} = -\Gamma_{\text{bottom}} = \int_0^{\infty}\int_0^{\pi} \omega_x(x=0, r, \theta) r\, dr\, d\theta = -\Gamma_0, \tag{18}$$

where $\Gamma_0 = R C_T U_h \cos^2\beta \sin\beta$ is the magnitude of the circulation strength. The corresponding induced mean velocity components on the transverse plane, v and w, can be obtained by applying the Biot-Savart law [15]

$$v = \begin{cases} -\dfrac{\Gamma_0}{4R}, & r \leqslant R \\ -\dfrac{\Gamma_0}{4R}\dfrac{R^2}{r^2}\cos(2\theta), & r > R, \end{cases} \qquad w = \begin{cases} 0, & r \leqslant R \\ -\dfrac{\Gamma_0}{4R}\dfrac{R^2}{r^2}\sin(2\theta), & r > R. \end{cases} \tag{19}$$

In order to compare the analytical solution in Eq. (17) with LES, it must first be filtered at scales commensurate with the LES grid resolution to be consistent with the filtered representation of the turbine forcing. This appropriate filtering was accomplished in Ref. [15] by first mapping Eq. (17) to an arc distributed along the turbine edges (actuator disk circumference) and then convolving this mapped function with a two-dimensional Gaussian filter. The resulting filtered vorticity at $x = 0$ is given by

$$\omega_x(\theta, r) = -\frac{\Gamma_0^*}{2R_*}\frac{\sin(\theta r/R_*)}{\sigma_R\sqrt{2\pi}} \exp\left(-\frac{(r-R_*)^2}{2\sigma_R^2}\right)\exp\left(-\frac{\sigma_R^2}{2R_*^2}\right), \tag{20}$$

where $R_* = R + 0.75h$ is the effective radius of the filtered actuator disk with h depending on the grid resolution according to $h = \sqrt{\Delta x^2 + \Delta y^2 + \Delta z^2}$. The Gaussian filter width is $\sigma_R = 1.5h/\sqrt{12}$. The magnitude of the effective circulation strength for the vortices expected from LES must be based on R_* instead of R, specifically, $\Gamma_0^* = R_* C_T U_h \cos^2\beta \sin\beta$. Further following Ref. [15], the analytical solutions for cross-stream induced velocities given by Eq. (19) are compared with the numerical solutions by plotting $v + u_r\cos\theta$ and $w + u_r\sin\theta$. Here, u_r is the radial velocity given by $u_r = (r/2)\partial_x u(R, 0, 0)$ for $r \leqslant R_*$ and $u_r = (R_*^2/2r)\partial_x u(R, 0, 0)$ for $r > R_*$. This step is done to eliminate the radial inflow that occurs due to streamtube expansion resulting from a finite streamwise pressure gradient behind the actuator disk that is not included in the theory but affects the LES results.

With these considerations, we can now compare the induced velocities from the LES including veer with the theory. The comparisons are shown in Fig. 6. Figure 6(a) shows contours of the streamwise vorticity from the LES of the CNBL with streamlines of the cross-stream velocities superimposed. The corresponding filtered values from the analytical model [Eq. (17)] are shown in

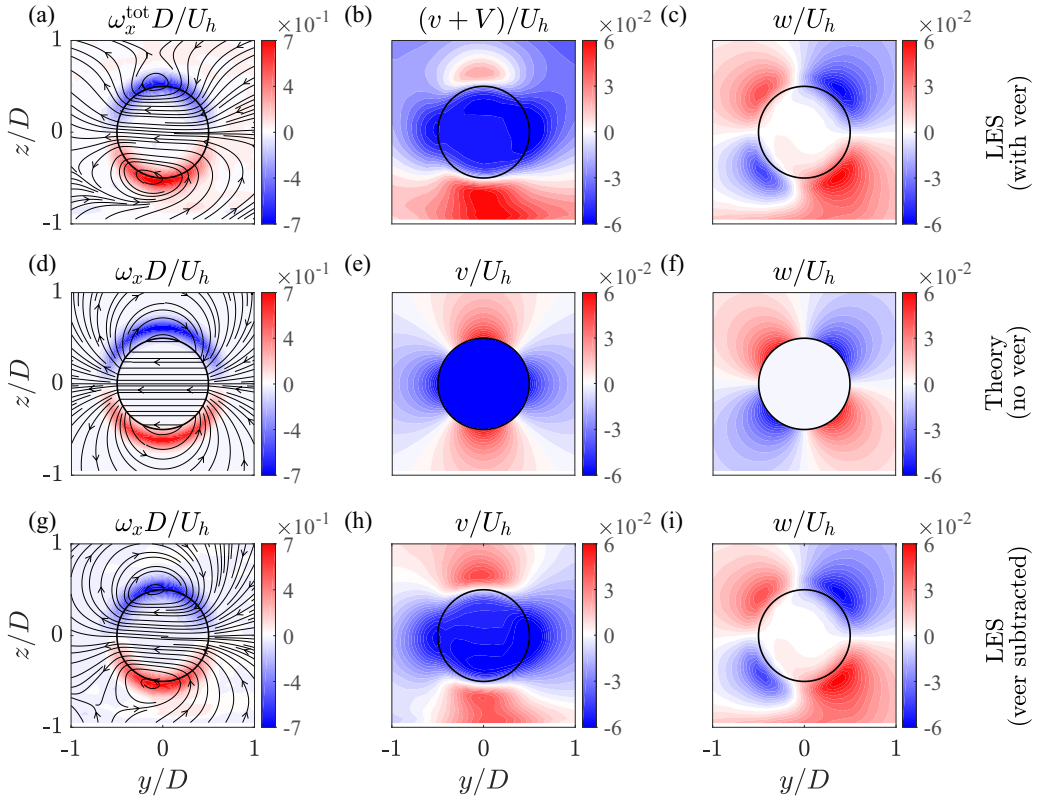

FIG. 6. Contours of $\omega_x^{\mathrm{tot}} D/U_h$ or $\omega_x D/U_h$ [(a), (d), and (g)], $(v+V)/U_h$ or v/U_h [(b), (e), and (h)], and w/U_h [(c), (f), and (i)] at $x/D = 0.5$ in the wake of a yawed turbine with $C_T' = 1.33$, $\beta = 20°$. (a)–(c) are from the CNBL LES, while (d)–(f) are analytical predictions [15]. Subtracting the veer component of vorticity and spanwise velocity from (a), (b), and (c) gives (g), (h), and (i), which has have good agreement with the analytical estimates [(d), (e), and (f)].

Fig. 6(d). The LES results displayed in Fig. 6(a) show a significant asymmetry. Here, most of the streamlines at the top do not close around the top vortex, in contrast to those of the bottom vortex. This difference from the symmetric behavior predicted by the theory is due to the background mean vorticity caused by the veer, $\Omega_x = -dV/dz$ and $\Omega_y = dU/dz$. This observation inspires a model in which the actual mean streamwise vorticity observed in LES (total vorticity ω_x^{tot}) comprises a linear superposition of the veer component of the vorticity (Ω_x) and the yawed turbine-generated vorticity (ω_x).

$$\omega_x^{\mathrm{tot}} = \omega_x + \Omega_x. \tag{21}$$

We note that for a TNBL there is no wind veer [$V(z) = 0$] and the mean streamwise vorticity is $\Omega_x = 0$. If the assumed form in (21) is correct, the difference $\omega_x^{\mathrm{tot}} - \Omega_x$ from LES (i.e., subtracting the veer vorticity $\Omega_x = -dV/dz$) should be well predicted by the theoretical vorticity distribution from Eq. (20). Figure 6(g) shows distributions of $\omega_x^{\mathrm{tot}} - \Omega_x$ from LES and its associated streamlines in the cross plane. Clearly, the agreement between the veer-subtracted CNBL LES data and the model is much improved. For example, the symmetry is recovered and the streamlines now close around the top vortex as expected from the model.

Figures 6(b), 6(e), and 6(h) show the corresponding spanwise mean velocities, while Figs. 6(c), 6(f), and 6(i) show the vertical velocities. The results in Fig. 6(b) show significant asymmetry. Since

$V > 0$ below the hub height and $V < 0$ above the hub height, the induced velocity above the rotor disk is significantly lower in the LES than in the model. In LES the veer velocity cancels much of the induced velocity from the yawed turbine. Upon subtracting the veer velocity distribution from the CNBL LES results [Figs. 6(g)–6(i)], we retrieve the more symmetric distribution, that has good agreement with the theory [Figs. 6(d)–6(f)]. Contours obtained from the LES of the TNBL case (not shown) also show good agreement with the model.

These results suggest that the model proposed in Ref. [15] to predict the generation of mean streamwise vorticity due to a yawed wind turbine remains essentially unaltered even in the presence of wind veer in a CNBL. The background veer vorticity can be added to that of the unperturbed vorticity distribution in order to model the total vorticity distribution immediately behind the yawed actuator disk. The further downstream evolution of mean vorticity is discussed in the following section.

B. Downstream evolution of mean vorticity

Downstream of the rotor, the streamwise evolution of the turbine-generated streamwise mean vorticity ω_x is dominated by mean advection and transverse turbulent diffusion [15],

$$U_h \frac{\partial \omega_x}{\partial x} = \nu_T(x)\left(\frac{\partial^2 \omega_x}{\partial y^2} + \frac{\partial^2 \omega_x}{\partial z^2}\right). \tag{22}$$

Here, $\nu_T(x) \sim u_\tau l(x)$ is the turbulent eddy viscosity, which can be modeled as the product of the friction velocity u_τ and a mixing length scale $l(x)$. The wake size, which increases linearly downstream of the turbine in the presence of ambient turbulence, is chosen as the appropriate mixing length scale, such that $l(x) \sim x$ [40]. Following Ref. [15], this linearly growing mixing length scale is given by $l(x) = 2\kappa_v(x - x_0)/\sqrt{24}$, where $k_v = u_\tau/U_h$ is the vortex expansion coefficient and $x_0 = -24^{-1/4}1.5h/k_v$ is the virtual origin. Using this $l(x)$, the eddy viscosity $\nu_T(x)$ becomes

$$\nu_T(x) = u_\tau 2k_v(x - x_0)/\sqrt{24}. \tag{23}$$

From the current LES simulations, using the values $u_\tau = 0.35$ m/s and $U_h = 6.4$ m/s, the vortex expansion coefficient for both simulations results in $k_v = 0.0547$.

We note that adding the constant vorticity due to veer, Ω_x to ω_x, does not affect Eq. (22) as long as it is constant in the vertical direction. Also, from Fig. 3, we can see that near the turbine, the magnitude of the veer velocity $V(z)$ is much smaller than the streamwise mean flow $U(z)$. Therefore we can expect the streamwise advection term to be dominant resulting in the same governing equation (15) for ω_x even in the presence of veer in a CNBL near the hub height. We note that advection of vorticity by the veer-affected mean velocity can be simply accounted for by interpreting x above as the streamline coordinate along the vortex trajectory that has a speed $V(z)$ in the transverse direction, but for now, we shall neglect these differences.

The solution to the advection-diffusion equation (22) can be obtained by linear superposition of the fundamental solution to the equation. The vorticity generated at the turbine can be regarded as a distribution of multiple point vortices with vorticity magnitude $d\omega_x(x = 0, y, z) = d\Gamma_p \delta(y - y_0)\delta(z - z_0)$ and circulation strength $d\Gamma_p$ located at the turbine disk edges $y_0 = R\cos\theta$, $z_0 = R\sin\theta$. Governed by Eq. (22), these point vortices are advected downstream by the mean flow with simultaneous turbulent diffusion along the transverse directions. Correspondingly, the fundamental solution [41] to Eq. (22) is

$$d\omega_x(x, y, z) = -\frac{d\Gamma_p}{4\pi^2\eta^2(x)} \exp\left(-\frac{(y - R\cos\theta)^2 + (z - R\sin\theta)^2}{4\eta^2(x)}\right), \tag{24}$$

where $\eta(x)$ is the transverse turbulent diffusion length scale [40] given by

$$\eta(x) = \sqrt{\frac{1}{U_h}\int_0^x \nu_T(\xi)\, d\xi}. \tag{25}$$

Using the eddy viscosity from (23) in (25), $\eta(x)$ becomes

$$\eta(x) = k_v(x - x_0)/24^{1/4}. \tag{26}$$

Adding the contributions from all the point vortices distributed on the turbine edge, the resultant downstream vorticity field is obtained. Adding this vorticity to that of the background veer leads to a total vorticity of

$$\omega_x^{\text{tot}}(x, y, z) = -\int_0^{2\pi} \frac{d\Gamma_p}{4\pi^2\eta^2(x)} \exp\left(-\frac{(y - R\cos\theta)^2 + (z - R\sin\theta)^2}{4\eta^2(x)}\right) + \Omega_x. \tag{27}$$

We assume that the peak vorticity occurs at $y = 0$ and $z = \pm R$; evaluating (27) at this location gives [15]

$$\omega_{x,\max}^{\text{tot}} = \frac{\Gamma_0}{4\eta^2(x)} \exp\left(-\frac{R^2}{2\eta^2(x)}\right) I_1\left(\frac{R^2}{2\eta^2(x)}\right) + \Omega_x, \tag{28}$$

where I_n is the nth-order modified Bessel function of the first kind.

The circulation strength $\Gamma(x)$ of the generated vorticity (excluding the background veer vorticity) as a function of the downstream location is obtained by integrating ω_x in the transverse plane, $\Gamma(x) = |\int_0^\infty \int_{-\infty}^\infty \omega_x(x, y, z)\, dy\, dz| = |\int_{-\infty}^0 \int_{-\infty}^\infty \omega_x(x, y, z)\, dy\, dz|$, which yields [15]

$$\frac{\Gamma(x)}{\Gamma_0} = \frac{\sqrt{\pi}}{4} \frac{R}{\eta(x)} \exp\left(-\frac{R^2}{8\eta^2(x)}\right)\left[I_0\left(\frac{R^2}{8\eta^2(x)}\right) + I_1\left(\frac{R^2}{8\eta^2(x)}\right)\right]. \tag{29}$$

These analytical predictions for the decay of the maximum vorticity and circulation strength were shown to have good agreement with the numerical simulations in Ref. [15].

In Fig. 7, the time-averaged streamwise vorticity distributions from the CNBL and TNBL simulations are plotted at different downstream locations; here, cross-stream velocity streamlines are superimposed. The results from the CNBL LES [i.e., including wind veer in Fig. 7(a)] can be compared with those with the veer subtracted [Fig. 7(b)] and the contours from the TNBL simulation [Fig. 7(c)]. Similar to prior results at the turbine location, it is evident from the cross-stream velocity streamlines that veer distorts the structure of the top and bottom vortices along their entire downstream evolution. This distortion results in an asymmetric distribution of vorticity between the top and bottom vortices.

Next, we compare the top and bottom vortex circulations from LES with the model. The circulation in LES is computed by integrating total vorticity $\Gamma_{\text{LES}}(x) = |\int_A \omega_x^{\text{tot}}(x, y, z)\, dy\, dz|$ over a suitably defined cross-sectional area A of the vortices. Following the approach of Ref. [15], we use Otsu's classification method to determine the cross-sectional region over which to integrate the vorticity. We apply the calculation of circulation both using the full vorticity and after subtracting the background veer vorticity.

The resulting decay of circulation for the CNBL case is shown in Fig. 8(a), where the unequal strength of the top (blue open circles) and bottom (red open circles) vortices can be seen. Veer causes the circulation strength of the bottom vortex to be significantly higher than the top vortex's circulation. Also, these circulation estimates deviate from the analytical prediction of Eq. (29) (solid curves in the plot). However, upon subtracting the veer vorticity Ω_x from the time-averaged vorticity (open triangles), we obtain good agreement with the theoretical estimate from (29) with small differences at far downstream locations for the bottom vortex. It also shows good agreement with the circulation strengths obtained from the TNBL simulation (crosses). Figure 8(b) shows that the peak vorticity of the CVP ($\omega_{x,\max}$) is much larger than the veer vorticity (Ω_x) so that whether the Ω_x is included or not does not affect the results appreciably.

In Fig. 8(a), we note a small deviation of the red open triangles at far downstream locations. This difference can be attributed to the size difference of the bottom vortex in the CNBL case versus the TNBL case [see Figs. 7(b) and 7(c) at $x/D = 8, 11$]. The difference could be due to a differing turbulent expansion rate of the vortices between the CNBL and TNBL cases. The presence

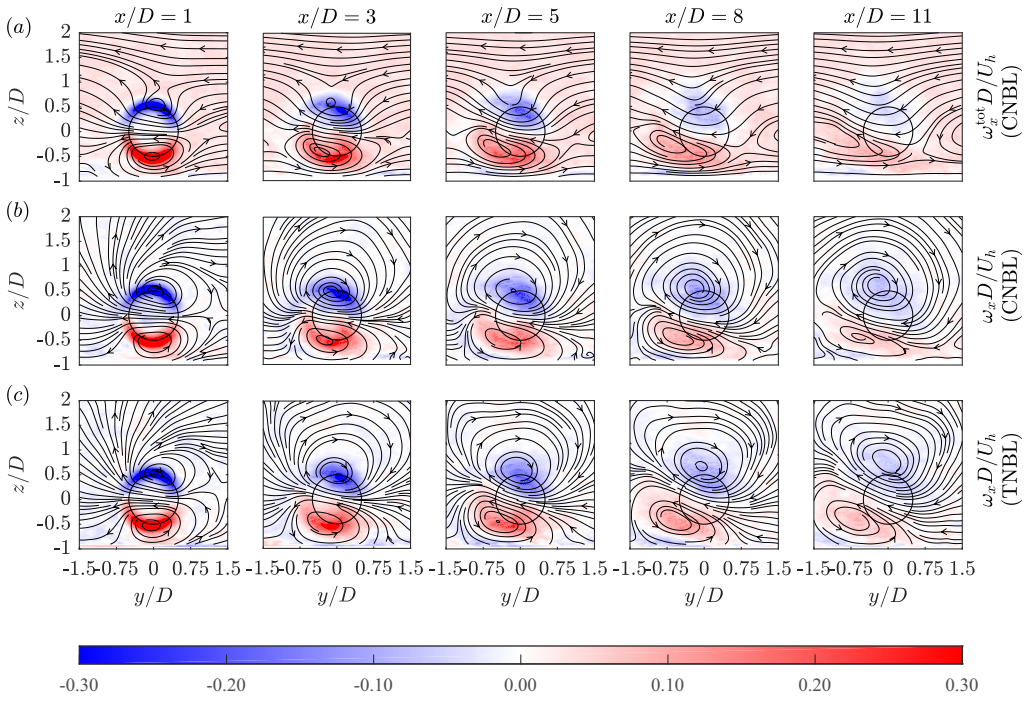

FIG. 7. Turbulent decay of streamwise vorticity (a) from the CNBL case with background veer, (b) from the CNBL case after subtracting the veer component, and (c) from the TNBL case at downstream locations $x/D = 1, 3, 5, 8, 11$.

of a capping inversion layer and the stable geostrophic region above a CNBL are known to limit the size of the largest turbulent eddies [42,43]. Thus turbulent diffusion may be more effective in the case of a TNBL, thus enlarging the bottom vortex more when compared with the CNBL. While the bottom vortices grow slightly differently in the TNBL and CNBL cases, the peak vorticity strengths

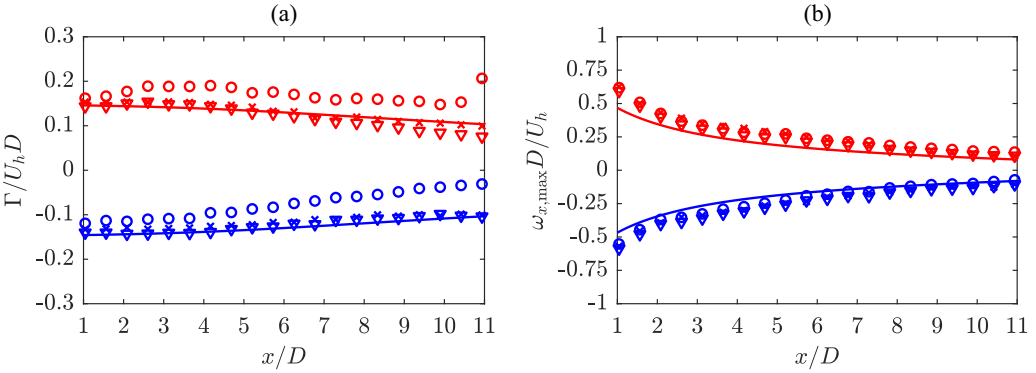

FIG. 8. Decay of (a) circulation strength $\Gamma/U_h D$ as a function of the downstream location and (b) maximum streamwise vorticity $\omega_{x,\max} D/U_h$ for the CNBL case. Red and blue colors correspond to bottom and top vortices of the CVP, respectively. Solid curves represent analytical solutions (28) and (29). Symbols represent quantities plotted from LES, where open circles include the wind veer component and open triangles are plotted after subtracting the wind veer component. Crosses are plotted from the TNBL simulation.

at downstream locations from Fig. 8(b) are quite comparable. Hence the circulation strength of the bottom vortex in a CNBL falls slightly below the analytical model due to its smaller size.

The comparisons of LES results with the theoretical model confirm that for the presently studied CNBL case the downstream evolution of mean vorticity remains dynamically unaffected by the presence of wind veer. The only effect of the veer is that its mean vorticity is superimposed with that of the vorticity generated by the yawed actuator disk. With improved understanding and an analytical model for the downstream evolution of vorticity in the wake of a yawed turbine, in the next section, we examine analytical modeling of the mean axial velocity deficit needed to predict the power generation of downstream wind turbines.

IV. APPLICATION OF VORTEX-SHEET-BASED CURLED WAKE MODEL IN A CNBL

The discussions in the previous sections demonstrate that a yawed actuator disk in the presence of an incoming mean flow sheds a pair of vortices behind the turbine. This CVP arises from an initially tubular vortex sheet distribution generated around the turbine disk periphery [13]. The induced velocity from the vortex sheet deflects the wake away from the centerline and also deforms the vortex sheet, leading to the known curled wake structure [9]. A recent study [16] proposes an analytical model for the downstream evolution of vorticity that reproduces the curled wake shape from the induced velocities acting on the vortex sheet. We first summarize the model of Ref. [16] in Sec. IV A. We then generalize it to include insights regarding effects of veer from the previous section and compare it with results from LES in Sec. IV B.

A. Summary of vortex-sheet-based curled wake model

According to the vortex-sheet-based curled wake model, the streamwise velocity deficit $\Delta u(x, y, z) = U(z) - u(x, y, z)$ is given by a Gaussian profile [10,44] according to

$$\frac{\Delta u}{U_h} = C(x) \exp\left[-\frac{(y - y_c)^2 + (z - z_h)^2}{2\,\sigma(\theta, x)^2} \right]. \tag{30}$$

Here, $C(x)$ is the magnitude of the normalized velocity deficit, while $\sigma(\theta, x)$ is the wake width expressed as a function of the downstream location x and polar angle θ defined as $\tan\theta = (z - z_h)/(y - y_c)$. The centroid location of the wake is y_c, z_h. In this section, we shift the origin of the $x\,y\,z$ coordinate system from the center of the turbine to the ground in order to be consistent with the curled wake model definitions in Ref. [16].

The wake width $\sigma(x, \theta)$ is determined by adding Jensen model linear wake growth [45] and the angle-dependent wake shape function according to

$$\sigma(\theta, x) = k_w x + 0.4\,\xi(\theta, x). \tag{31}$$

Here, $k_w = 0.6u_\tau/U_h$ is the wake expansion coefficient [16], and the curled structure of the wake is modeled by the angle-dependent wake shape function $\xi(\theta, x)$. This function describes the vortex sheet location that augments the wake width along the polar angle θ at any given streamwise location as per Eq. (31). The sketches in Fig. 9 show the shape of the wake behind the turbine under different conditions. Figure 9(a) shows the symmetric Gaussian wake of an unyawed turbine that expands linearly downstream of the flow in a TNBL without wind veer effects. Figure 9(b) shows the definition of the angle-dependent wake shape function $\xi(\theta, x)$, which becomes curled due to the vortex sheet self-induction again in the absence of wind veer. Figure 9(c) shows a sketch of the wake behind a yawed turbine in an ABL with wind veer effects, which is further discussed in Sec. IV B. The model in Ref. [16] also takes into account the effect of the hub vortex which occurs as a result of the rotation of the turbine. However, in this paper, we do not include the effects of rotation.

The wake shape function $\xi(\theta, x)$ has units of length and is normalized using $\xi_0(\theta) = \xi(\theta, 0)$, the initial shape of the wake, which depends on the angle θ and represents the shape of an ellipse as the

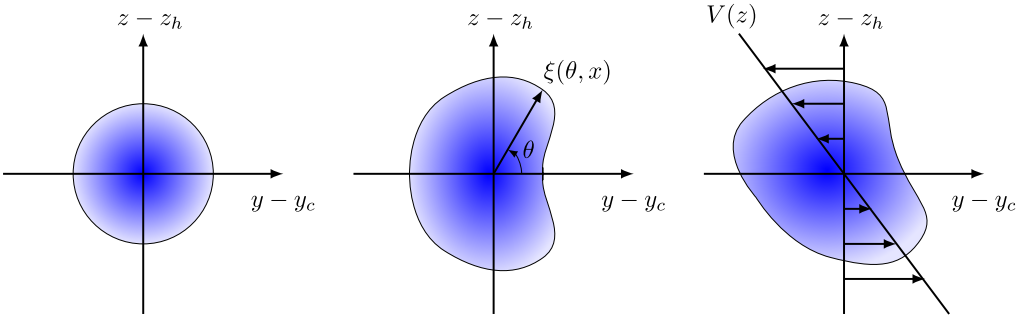

(a) $\beta = 0, V(z) = 0$ (b) $\beta \neq 0, V(z) = 0$ (c) $\beta \neq 0, V(z) = -S(z - z_h)$

FIG. 9. Sketch of velocity deficit behind (a) an unyawed turbine with no wind veer, (b) a yawed turbine showing the induced curled wake, with the angle-dependent wake shape function $\xi(\theta, x) = \xi_0(\theta)\hat{\xi}(\theta, \hat{t})$ and no wind veer, and (c) the yawed turbine in a CNBL (with wind veer). The shading represents the strength of the velocity deficit Δu.

rotor disk is yawed

$$\xi_0(\theta) = R\sqrt{A_*}\frac{|\cos\beta|}{\sqrt{1 - \sin^2\beta\sin^2\theta}}. \tag{32}$$

Here, A_* is the ratio of the expanded streamtube area with the projected frontal area of the rotor [16]:

$$A_* = \frac{1 + \sqrt{1 - C_T\cos^2\beta}}{2\sqrt{1 - C_T\cos^2\beta}}. \tag{33}$$

The normalization introduces a dimensionless angle-dependent wake shape function $\hat{\xi}(\theta, \hat{t})$ according to

$$\xi(\theta, x) = \xi_0(\theta)\hat{\xi}(\theta, \hat{t}), \tag{34}$$

where $\hat{t}$ is a dimensionless time variable to be defined below [16].

The downstream evolution of the angle-dependent radial location of the wake is given by $\xi(\theta, x) = \xi_0(\theta) + \int u_r(\theta, t)\,dt$, where time t indicates the downstream evolution, i.e., $t = x/U_h$, and $u_r(\theta, t)$ is the radial velocity induced by the shed streamwise vorticity. The vortex sheet shape at downstream locations for a given θ is changed by the induced radial velocity from the vortices. Given the strength of the vortex sheet or the circulation density $\gamma = \gamma(\theta, t)$, the radial velocity $u_r(\theta, t)$ governing the shape of the vortex sheet can be determined using the Biot-Savart law as described in Ref. [16]. In Ref. [16], the evolution of dimensionless velocities, $\hat{u}_r = u_r/\gamma_b$, $\hat{u}_\theta = u_\theta/\gamma_b$, and sheet location, $\hat{\xi} = \xi/\xi_0$, is obtained using a power series method, where γ_b is the reference circulation density at the turbine location. It is related to the circulation strength Γ_0 in Eq. (18) by

$$\gamma_b = \frac{\Gamma_0}{2R} = \frac{1}{2}C_T U_h\cos^2\beta\sin\beta. \tag{35}$$

The dimensionless time is defined as $\hat{t} = t\,\gamma_b/\xi_0$. These analytical general solutions are valid at short times, i.e., only near the turbine for times $|\hat{t}| \leqslant 2$ [16].

To capture the wake-curling effects at large times, an empirical expression for the nondimensional vortex sheet location $\hat{\xi}(\theta, \hat{t})$ is proposed (see Eq. (B1) in Ref. [16]) which is valid for both

short and long times. For a nonrotating turbine, the empirical expression simplifies to

$$\hat{\xi}(\theta,\hat{t}) = 1 - \alpha\left[\frac{1}{2}\tanh\left(\frac{\hat{t}^2}{4\alpha}\right)\cos 2\theta - \frac{1}{4}\tanh\left(\frac{\hat{t}^3}{8\alpha}\right)\cos(3\theta) - \frac{5}{48}\tanh\left(\frac{\hat{t}^4}{16\alpha}\right)\cos(2\theta) + \frac{7}{48}\tanh\left(\frac{\hat{t}^4}{16\alpha}\right)\cos(4\theta)\right], \tag{36}$$

where the constant $\alpha = 1.263$. In Eq. (36), we also need to know $\hat{t}$. In a turbulent boundary layer, the strength of the vortex decays downstream leading to a time-dependent circulation density $\gamma_b = \gamma_b(t)$ [16]. The definition of the nondimensional time $\hat{t} = t\gamma_b/\xi_0$ then generalizes to

$$\hat{t} = \frac{1}{\xi_0}\int_0^t \gamma_b(t')\,dt'. \tag{37}$$

The circulation density $\gamma_b(t)$ is related to the decaying circulation strength $\Gamma(x)$ considered in Eq. (29) by $\gamma_b = \Gamma(x)/2R$. Using this relation along with $t \approx x/U(z)$ with $U(z) = (u_\tau/\kappa)\ln(z/z_0)$ and $\eta(x) = k_v x/24^{1/4}$ from Eq. (26), and assuming the virtual origin $x_0 = 0$ to simplify the problem, the integral (37) becomes

$$\hat{t} = \frac{24^{1/4}}{2k_v U(z)\xi_0 R}\int_0^\eta \Gamma_b(\eta')\,d\eta'. \tag{38}$$

The integral was approximated using a fitting function resulting in a $\hat{t}$ which is expressed compactly according to

$$\hat{t}(x,z) \approx -1.44\frac{U_h}{u_\tau}\frac{R}{R\sqrt{A_*}}C_T\cos^2\beta\sin\beta\left[1 - \exp\left(-0.35\frac{u_\tau}{U(z)}\frac{x}{R}\right)\right]. \tag{39}$$

The value of $\hat{t}$ from Eq. (39) is used to evaluate $\hat{\xi}(\theta,\hat{t})$ in (36) and subsequently obtain $\xi(\theta,x) = \xi_0(\theta)\hat{\xi}(\theta,\hat{t})$ in Eq. (31).

Next, we turn to the normalized maximum velocity deficit magnitude $C(x) = \Delta u_{\max}/U_h$ in Eq. (30), which is given by

$$C(x) = 1 - \sqrt{1 - \frac{C_T\cos^3\beta}{2\tilde{\sigma}^2(x)/R^2}}, \tag{40}$$

where

$$\tilde{\sigma}^2(x) = (k_w x + 0.4R\sqrt{A_*})(k_w x + 0.4R\sqrt{A_*}\cos\beta) \tag{41}$$

is an estimate of the average wake width over the angles which captures the trend of reduction of horizontal width due to yawing at an angle β. The quantity $R\sqrt{A_*}$ is also an approximation of the initial wake shape according to Eq. (32) for small β.

In Fig. 5, this analytical prediction for the maximum normalized velocity deficit magnitude $C(x)$ is plotted alongside estimates from the CNBL and TNBL LES. Here it is clear that the model provides good agreement with the LES and is able to predict the correct velocity deficit decay for $x/D \gtrsim 3$.

The curled wake model predicts the wake deflection y_c due to the shed vorticity according to

$$y_c = \hat{y}_c(\hat{t})R\sqrt{A_*}, \tag{42}$$

where the nondimensional wake deflection $\hat{y}_c$ is expressed as

$$\hat{y}_c(\hat{t}) = \frac{(\pi-1)|\hat{t}|^3 + 2\sqrt{3}\pi^2\hat{t}^2 + 48(\pi-1)^2|\hat{t}|}{2\pi(\pi-1)\hat{t}^2 + 4\sqrt{3}\pi^2|\hat{t}| + 96(\pi-1)^2}\mathrm{sgn}(\hat{t}) - \frac{2}{\pi}\frac{\hat{t}}{[(z+z_h)/R\sqrt{A_*}]^2 - 1}. \tag{43}$$

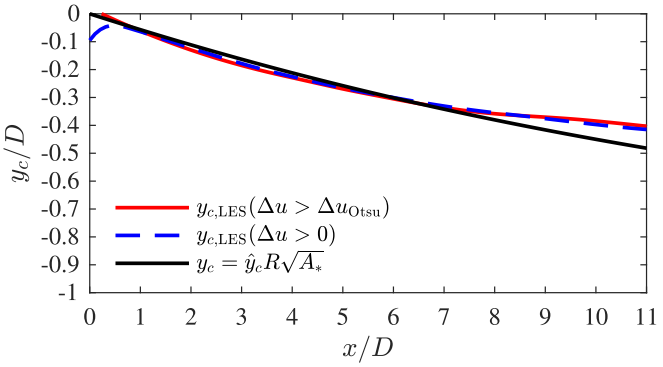

FIG. 10. The wake deflection at hub height from the LES (CNBL) determined using two different methods is compared with the estimate from the curled wake model (black solid curve) [16]. The LES results include $y_{c,\mathrm{LES}}$ using the integration over the positive velocity defect region (blue dashed curve) or Otsu's method (red solid curve).

In Ref. [16], an analytical solution for the wake deflection for short times is obtained assuming a circular vortex sheet. For longer times, the deflection of the wake is estimated instead by modeling the vorticity distribution as a CVP. This first term in Eq. (43) which is an empirical fit captures the behavior of both these solutions across short and long times. The second term models the deflection due to the image vortices needed to model ground effects.

These analytical estimates for wake deflection in Eq. (42) are compared with the wake deflection computed from the velocity deficit in the CNBL simulation in Fig. 10. The blue dashed curve and red solid curve represent the wake deflection $y_{c,\mathrm{LES}}$ obtained from the CNBL simulation using

$$y_{c,\mathrm{LES}}(x) = \frac{\int_y y\ \Delta u(x, y, z_h)\, dy}{\int_y \Delta u(x, y, z_h)\, dy}, \tag{44}$$

where $\Delta u(x, y, z) = U(z) - u(x, y, z)$ is the velocity deficit. We chose two methods, one in which regions where $\Delta u > 0$ are used to perform the integrations in Eq. (44) and another in which regions where $\Delta u > \Delta u_{\mathrm{Otsu}}$ are used. Here, Δu_{Otsu} is the threshold chosen by the Otsu edge detection method [15]. It is evident in Fig. 10 that the wake deflection from the curled wake model given by Eq. (42) shows good agreement with the LES up to $x/D = 7$ but slightly overpredicts the observed deflection further downstream. For the purposes of the present modeling accuracy, however, we consider the level of agreement satisfactory.

B. Curled wake model applied to the CNBL including veer

Following Ref. [20], the effect of veer can be included as an additional spanwise wake displacement such that

$$y_{c,\mathrm{veer}}(x, z) = \frac{x}{U(z)} V(z) \approx -\frac{x}{U(z)} S\,(z - z_h). \tag{45}$$

Here, we also take into account the additional effects from z-dependent streamwise velocity. This effect induces larger sideways displacement in the lower parts of the domain since for a fixed x, the advection time will be larger and the sideways displacement will have had more "time" to take place. The total spanwise wake deflection of the velocity deficit in (30) including the veer displacement (45) is

$$y_c(x, z) = \hat{y}_c(\hat{t})\, R\sqrt{A_*} - \frac{x}{U(z)} S\,(z - z_h), \tag{46}$$

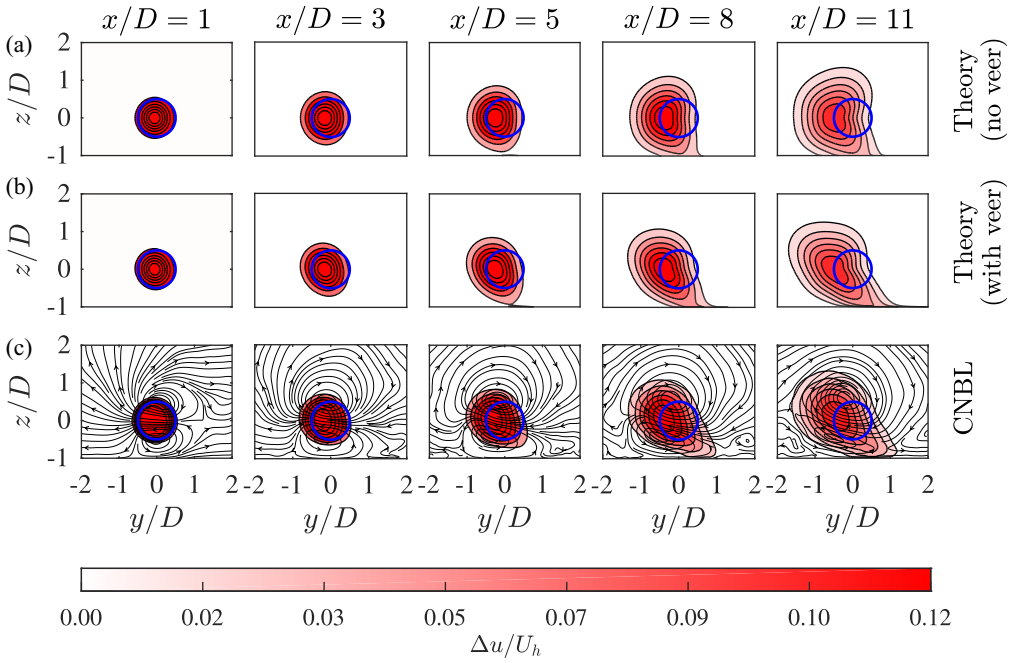

FIG. 11. Contours of $\Delta u/U_h$ at various streamwise locations from curled wake analytical model (30) with centroid locations (a) $y_c = \hat{y}_c(\hat{t})R\sqrt{A_*}$ (no veer correction) and (b) $y_c = \hat{y}_c(\hat{t})R\sqrt{A_*} + y_{c,\text{veer}}$ (with veer correction). (c) the CNBL simulation with the v-w velocity streamlines.

where $\hat{y}_c(\hat{t})$ is the dimensionless deflection given by Eq. (43) with $\hat{t} = \hat{t}(x, z)$ evaluated from Eq. (39). For the present LES data, the shear rate S of the wind veer in Eq. (45) has been measured, and results in $S = 2.2\times10^{-3}$ s^{-1} [see Fig. 3(c)].

Analytical model predictions for $\Delta u/U_h$ from Eq. (30) at select downstream distances are plotted as contours in Fig. 11(a) (no veer) and Fig. 11(b) (including veer) and compared against the CNBL data [Fig. 11(c)]. Figure 11(c) also includes v-w cross-stream velocity streamlines (evaluated from LES with the veer velocity subtracted). In Figs. 12 and 13, the one-dimensional profiles of $\Delta u/U_h$ at $z/D = [0.36, 1, 1.59]$ and $y/D = [-0.94, 0, 0.42]$, respectively, are plotted at different downstream locations. We can clearly see the effect of the wind veer in the contours of the analytically modeled defect velocity. The veer deflects the wake rightward below the hub height and leftward above the hub height, whereas not including the veer produces a wake that is only deformed by the vortex sheet streamwise vorticity, resulting in a curled wake structure. The analytically predicted contours closely resemble the contours from the CNBL simulation. The one-dimensional profiles in Figs. 12 and 13 show a more detailed comparison between the model and LES. These plots show that the veer-deflected velocity deficit structure at far downstream locations is better predicted by the wake model with the veer correction term included, albeit with slight deviations.

The results suggest that the curled wake model which was originally developed for a TNBL can also be applied to a CNBL. The presence of veer only alters the shape of the velocity deficit by shifting it towards one side below the hub height and to the other side above the hub height, and this effect can be modeled with the additional spanwise deflection term given by Eq. (45).

To complete the description of velocity defect evolution, we compare with results from the TNBL simulation in Fig. 14, again including the cross-stream velocity streamlines. Although there is no wind veer in this simulation, we observe that the wake structure is still deflected to the right below the hub height and somewhat towards the left above the hub height. This may appear surprising at first sight since one would expect that the CVP induces a symmetric curled wake structure akin

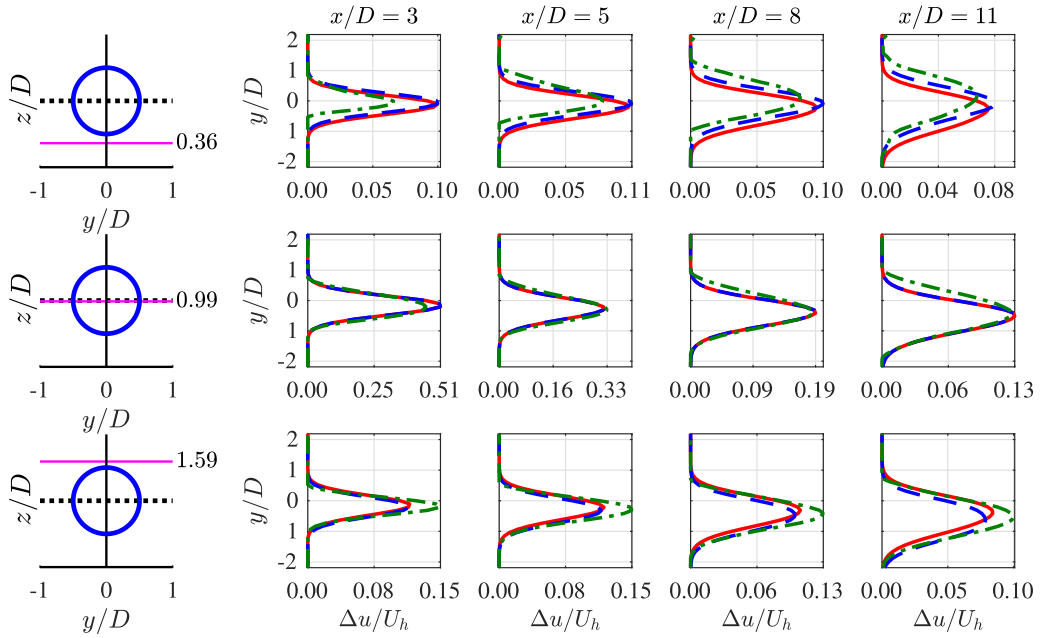

FIG. 12. Profiles of $\Delta u/U_h$ plotted at $z/D = [0.36, 1, 1.59]$ and different streamwise locations $x/D = [3, 5, 8, 11]$ from the curled wake analytical model (30) with centroid locations $y_c = \hat{y}_c(\hat{t})R\sqrt{A_*}$ (red solid curves) and $y_c = \hat{y}_c(\hat{t})R\sqrt{A_*} + y_{c,\text{veer}}$ (blue dashed curves), and the CNBL simulation (green dash-dotted curves).

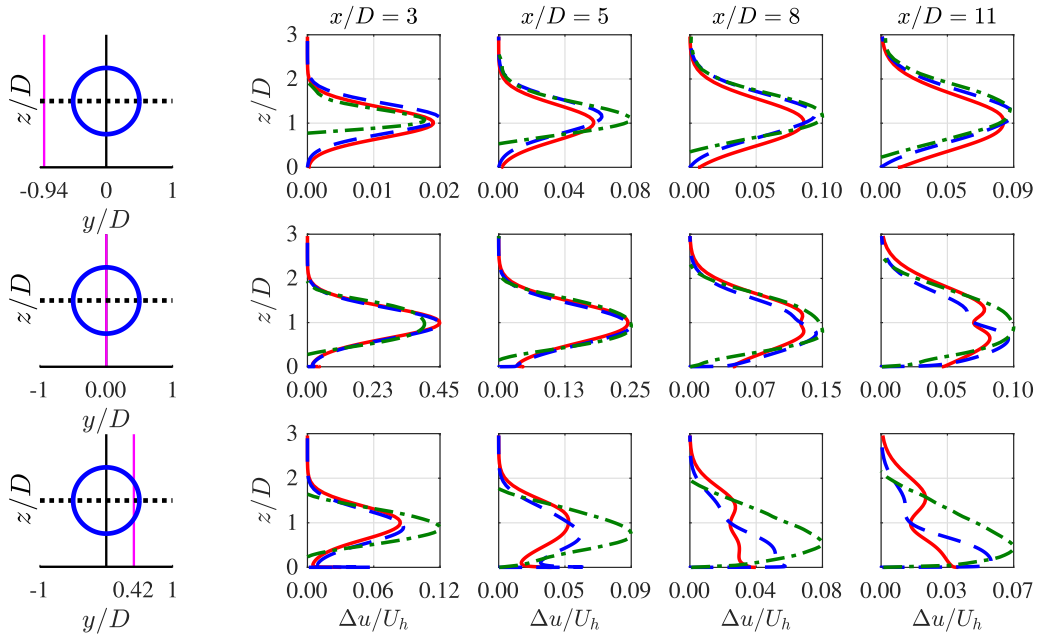

FIG. 13. Profiles of $\Delta u/U_h$ plotted at $y/D = [-0.94, 0, 0.42]$ and different streamwise locations $x/D = [3, 5, 8, 11]$ from the curled wake analytical model (30) with centroid locations $y_c = \hat{y}_c(\hat{t})R\sqrt{A_*}$ (red solid curves) and $y_c = \hat{y}_c(\hat{t})R\sqrt{A_*} + y_{c,\text{veer}}$ (blue dashed curves), and the CNBL simulation (green dash-dotted curves).

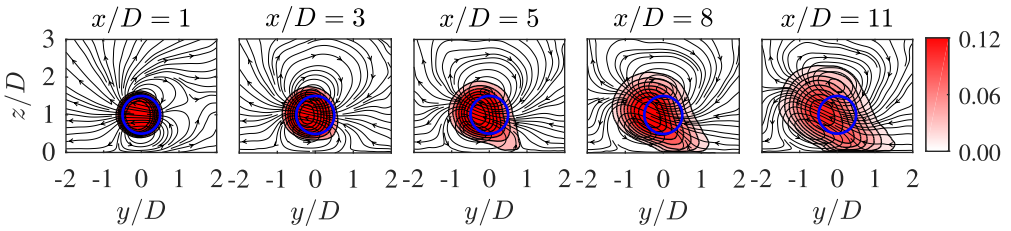

FIG. 14. Contours of $\Delta u/U_h$ from the TNBL simulation with cross-stream v-w velocity streamlines.

to the analytical contours from Fig. 11(a) without veer. However, in this case, the cause for the asymmetry appears to be that unlike what is assumed in the model, the top and bottom vortices themselves are not aligned in the same spanwise location. We can clearly see from the contour at $x/D = 11$ in Fig. 14 that the bottom vortex has moved relatively more towards the left than the top vortex. The cause of the misalignment of the two vortices is likely due to the fact that the streamwise advection velocity near the ground is smaller than that at the top due to the shear in the $U(z)$ ABL profile. Thus, at a fixed distance x from the turbine, moving with the mean velocity there has been more time for a sideways motion for the bottom vortex (induced by the top vortex) as compared with the top vortex (induced by the bottom vortex). As a result, the entire bottom vortex is shifted to the left, hence deflecting the induced velocity near the wake center downwards. This effect is partially accounted for by using $U(z)$ in Eq. (39) in the model and hence also helps explain the slight top-bottom asymmetry seen in Fig. 11(a) even in the absence of veer. However, the results show that for the TNBL case this effect is somewhat stronger. More detailed model versions that take such effects into account may have to be developed. However, the presently proposed approach already provides significant accuracy in predicting the highly nontrivial spatial distribution of velocity in yawed turbine wakes.

V. CONCLUSIONS

This study investigates the effect of wind veer on the evolution of mean streamwise vorticity and velocity deficit in the wake of a yawed turbine, in the context of CNBLs including Coriolis acceleration causing a wind veer. In earlier work in the absence of veer (TNBL), the curled wake dynamics had been shown to be best understood as consisting of a vortex generation phase, where streamwise vorticity is injected in the flow due to the curl of the turbine yaw force, followed by downstream advection and transverse turbulent diffusion of vorticity. Analytical solutions describing such behavior were derived and validated in Ref. [15]. In this paper, we have shown that the evolution of mean vorticity remains relatively unchanged even in the presence of wind veer. LES data show that when wind veer is included, the streamwise vorticity corresponding to the veering mean flow, Ω_x, is simply superimposed additively to the vorticity generated by the yawed turbine. For the yaw angle considered in this paper, this strengthens the bottom vortex and weakens the top vortex while their evolution is still modeled well following the approach as described in Ref. [15]. We also adapted the vortex-sheet-based curled wake model [16] to describe present flow conditions. It was found to yield good results for modeling the velocity deficit in both conventionally neutral and truly neutral conditions. The velocity deficit affects downstream wind turbines if interacting with the wake. The presence of wind veer in the CNBL can be included in the wake model by adding an additional spanwise displacement term, modeled here using the wind veer velocity $V(z)$. We approximated the latter as $V(z) = -S(z - z_h)$, where the shear rate parameter S was determined from the LES of CNBL flow. Although only one yaw angle is discussed in this paper, the veer correction can in principle be applied to model the evolution of the velocity deficit for different yaw angles, at least up to those tested in the work of Ref. [16], i.e., up to $\beta = 30^0$. Also, note that neither the LES nor the model proposed includes the effects of wake angular momentum. Such effects can

be included in the analytical model as well as in the LES using ADM with rotation (ADM-R), as was done in Ref. [16]. A detailed analysis of such additional effects, i.e., evaluating whether wake angular momentum could affect the superposition of veer and yaw vorticity decay, is left for future efforts. For a fully predictive analytical model, one requires, in addition, an analytical model for $V(z)$ and $U(z)$. Further work is required to cast such models (e.g., those developed in Refs. [46,47]) in terms that can be efficiently incorporated into present wind turbine wake models.

ACKNOWLEDGMENTS

This research has been supported by the National Science Foundation (Grant No. CBET-1949778). We are thankful to the National Center for Atmospheric Research (NCAR) for providing the computational resources. Discussions with Dr. C. Shapiro are greatly appreciated.

[1] P. Fleming, J. King, K. Dykes, E. Simley, J. Roadman, A. Scholbrock, P. Murphy, J. K. Lundquist, P. Moriarty, K. Fleming, J. van Dam, C. Bay, R. Mudafort, H. Lopez, J. Skopek, M. Scott, B. Ryan, C. Guernsey, and D. Brake, Initial results from a field campaign of wake steering applied at a commercial wind farm – Part 1, Wind Energy Sci. **4**, 273 (2019).

[2] M. F. Howland, S. K. Lele, and J. O. Dabiri, Wind farm power optimization through wake steering, Proc. Natl. Acad. Sci. USA **116**, 14495 (2019).

[3] I. Grant, P. Parkin, and X. Wang, Optical vortex tracking studies of a horizontal axis wind turbine in yaw using laser-sheet, flow visualisation, Exp. Fluids **23**, 513 (1997).

[4] I. Grant and P. Parkin, A DPIV study of the trailing vortex elements from the blades of a horizontal axis wind turbine in yaw, Exp. Fluids **28**, 368 (2000).

[5] P. Parkin, R. Holm, and D. Medici, The application of PIV to the wake of a wind turbine in yaw, in *Particle Image Velocimetry, Göttingen, 17 September 2001 through 19 September 2001*, edited by J. Kompenhans, DLR Mitteilung Vol. 3 (DLR Institute of Aerodynamics and Flow Technology, Göttingen, 2001), pp. 155–162.

[6] W. Haans, T. Sant, G. van Kuik, and G. van Bussel, Measurement of tip vortex paths in the wake of a HAWT under yawed flow conditions, J. Solar Energy Eng. **127**, 456 (2005).

[7] D. Medici and P. H. Alfredsson, Measurements on a wind turbine wake: 3D effects and bluff body vortex shedding, Wind Energy **9**, 219 (2006).

[8] Á. Jiménez, A. Crespo, and E. Migoya, Application of a LES technique to characterize the wake deflection of a wind turbine in yaw, Wind Energy **13**, 559 (2010).

[9] M. F. Howland, J. Bossuyt, L. A. Martínez-Tossas, J. Meyers, and C. Meneveau, Wake structure in actuator disk models of wind turbines in yaw under uniform inflow conditions, J. Renewable Sustainable Energy **8**, 043301 (2016).

[10] M. Bastankhah and F. Porté-Agel, Experimental and theoretical study of wind turbine wakes in yawed conditions, J. Fluid Mech. **806**, 506 (2016).

[11] C. R. Shapiro, D. F. Gayme, and C. Meneveau, Modelling yawed wind turbine wakes: a lifting line approach, J. Fluid Mech. **841**, R1 (2018).

[12] L. A. Martínez-Tossas, J. Annoni, P. A. Fleming, and M. J. Churchfield, The aerodynamics of the curled wake: a simplified model in view of flow control, Wind Energy Sci. **4**, 127 (2019).

[13] L. A. Martínez-Tossas and E. Branlard, The curled wake model: equivalence of shed vorticity models, in *NAWEA WindTech 2019, 14–16 October 2019, Amherst, MA USA*, Journal of Physics: Conference Series Vol. 1452 (Institute of Physics, London, 2020), p. 012069.

[14] H. Zong and F. Porté-Agel, A point vortex transportation model for yawed wind turbine wakes, J. Fluid Mech. **890**, A8 (2020).

[15] C. R. Shapiro, D. F. Gayme, and C. Meneveau, Generation and decay of counter-rotating vortices downstream of yawed wind turbines in the atmospheric boundary layer, J. Fluid Mech. **903**, R2 (2020).

[16] M. Bastankhah, C. R. Shapiro, S. Shamsoddin, D. F. Gayme, and C. Meneveau, A vortex sheet based analytical model of the curled wake behind yawed wind turbines, J. Fluid Mech. **933**, A2 (2022).
[17] M. Abkar and F. Porté-Agel, Influence of atmospheric stability on wind-turbine wakes: A large eddy simulation study, Phys. Fluids **27**, 035104 (2015).
[18] V. W. Ekman, On the influence of the Earth's rotation on ocean-currents, Ark. Mat., Astron. Fys. **2**, 11 (1905).
[19] S. N. Gadde and R. J. Stevens, Effect of Coriolis force on a wind farm wake, in *Wake Conference 2019, 22–24 May 2019, Visby, Sweden*, Journal of Physics: Conference Series Vol. 1256 (Institute of Physics, London, 2019), p. 012026.
[20] M. Abkar, J. N. Sørensen, and F. Porté-Agel, An analytical model for the effect of vertical wind veer on wind turbine wakes, Energies **11**, 1838 (2018).
[21] M. F. Howland, C. M. González, J. J. P. Martínez, J. B. Quesada, F. P. Larrañaga, N. K. Yadav, J. S. Chawla, and J. O. Dabiri, Influence of atmospheric conditions on the power production of utility-scale wind turbines in yaw misalignment, J. Renewable Sustainable Energy **12**, 063307 (2020).
[22] D. Allaerts and J. Meyers, Large eddy simulation of a large wind-turbine array in a conventionally neutral atmospheric boundary layer, Phys. Fluids **27**, 065108 (2015).
[23] https://lesgo.me.jhu.edu.
[24] J. D. Albertson and M. B. Parlange, Surface length scales and shear stress: Implications for land-atmosphere interaction over complex terrain, Water Resour. Res. **35**, 2121 (1999).
[25] E. Bou-Zeid, C. Meneveau, and M. Parlange, A scale-dependent Lagrangian dynamic model for large eddy simulation of complex turbulent flows, Phys. Fluids **17**, 025105 (2005).
[26] R. J. Stevens, J. Graham, and C. Meneveau, A concurrent precursor inflow method for large eddy simulations and applications to finite length wind farms, Renewable Energy **68**, 46 (2014).
[27] M. Calaf, C. Meneveau, and J. Meyers, Large eddy simulation study of fully developed wind-turbine array boundary layers, Phys. Fluids **22**, 015110 (2010).
[28] M. Calaf, M. B. Parlange, and C. Meneveau, Large eddy simulation study of scalar transport in fully developed wind-turbine array boundary layers, Phys. Fluids **23**, 126603 (2011).
[29] R. J. A. M. Stevens, D. F. Gayme, and C. Meneveau, Large eddy simulation studies of the effects of alignment and wind farm length, J. Renewable Sustainable Energy **6**, 023105 (2014).
[30] L. A. Martínez-Tossas, M. J. Churchfield, and C. Meneveau, Large Eddy Simulation of wind turbine wakes: detailed comparisons of two codes focusing on effects of numerics and subgrid modeling, in *Wake Conference 2015, 9–11 June 2015, Visby, Sweden*, Journal of Physics: Conference Series Vol. 625 (Institute of Physics, London, 2015), p. 012024.
[31] C. R. Shapiro, D. F. Gayme, and C. Meneveau, Filtered actuator disks: Theory and application to wind turbine models in large eddy simulation, Wind Energy **22**, 1414 (2019).
[32] A. Sescu and C. Meneveau, A control algorithm for statistically stationary large eddy simulations of thermally stratified boundary layers, Q. J. R. Meteorol. Soc. **140**, 2017 (2014).
[33] R. Stoll and F. Porté-Agel, Dynamic subgrid-scale models for momentum and scalar fluxes in large eddy simulations of neutrally stratified atmospheric boundary layers over heterogeneous terrain, Water Resour. Res. **42**, W01409 (2006).
[34] W. Munters, C. Meneveau, and J. Meyers, Shifted periodic boundary conditions for simulations of wall-bounded turbulent flows, Phys. Fluids **28**, 025112 (2016).
[35] J. Meyers and C. Meneveau, Large eddy simulations of large wind-turbine arrays in the atmospheric boundary layer, in *48th AIAA Aerospace Sciences Meeting Including the New Horizons Forum and Aerospace Exposition* (American Institute of Aeronautics and Astronautics, Reston, VA, 2010), p. AIAA 2010-827
[36] L. Martinez, S. Leonardi, M. Churchfield, and P. Moriarty, A comparison of actuator disk and actuator line wind turbine models and best practices for their use, in *50th AIAA Aerospace Sciences Meeting Including the New Horizons Forum and Aerospace Exposition* (American Institute of Aeronautics and Astronautics, Reston, VA, 2012), p. AIAA 2012-0900
[37] D. Allaerts and J. Meyers, Boundary-layer development and gravity waves in conventionally neutral wind farms, J. Fluid Mech. **814**, 95 (2017).

[38] D. R. Durran and J. B. Klemp, A compressible model for the simulation of moist mountain waves, Mon. Weather Rev. **111**, 2341 (1983).
[39] L. A. Martínez-Tossas, M. J. Churchfield, and C. Meneveau, Optimal smoothing length scale for actuator line models of wind turbine blades based on Gaussian body force distribution, Wind Energy **20**, 1083 (2017).
[40] C. R. Shapiro, G. M. Starke, C. Meneveau, and D. F. Gayme, A wake modeling paradigm for wind farm design and control, Energies **12**, 2956 (2019).
[41] P. G. Saffman, *Vortex Dynamics, Cambridge Monographs on Mechanics* (Cambridge University Press, Cambridge, 1993).
[42] S. A. Kitaigorodskii and S. M. Joffre, In search of a simple scaling for the height of the stratified atmospheric boundary layer, Tellus, Ser. A: Dynamic Meteorol. Oceanogr. **40**, 419 (1988).
[43] J. C. Wyngaard, *Turbulence in the Atmosphere* (Cambridge University Press, Cambridge, 2010).
[44] M. Bastankhah and F. Porté-Agel, A new analytical model for wind-turbine wakes, Renewable Energy **70**, 116 (2014).
[45] N. Jensen, *A note on wind generator interaction*, Risø-M No. 2411, Risø National Laboratory, 1983.
[46] K. Krishna, The planetary-boundary-layer model of Ellison (1956)—A retrospect, Boundary-Layer Meteorol. **19**, 293 (1980).
[47] B. Cushman-Roisin and V. Malacic, Bottom Ekman pumping with stress-dependent eddy viscosity, J. Phys. Oceanogr. **27**, 1967 (1997).